PHOTONICS Research

Silicon photonic platforms for mid-infrared applications [Invited]

Ting Hu,[1] Bowei Dong,[1,2] Xianshu Luo,[1,*] Tsung-Yang Liow,[1] Junfeng Song,[1] Chengkuo Lee,[2] and Guo-Qiang Lo[1]

[1]Institute of Microelectronics, Agency for Science, Technology and Research (A*STAR), 2 Fusionopolis Way, #08-02, Innovis, Singapore 138634, Singapore
[2]Department of Electrical & Computer Engineering, National University of Singapore, 4 Engineering Drive 3, Singapore 117583, Singapore
*Corresponding author: luox@ime.a-star.edu.sg

Received 5 June 2017; revised 11 July 2017; accepted 12 July 2017; posted 12 July 2017 (Doc. ID 297458); published 17 August 2017

Silicon photonic integrated circuits for telecommunication and data centers have been well studied in the past decade, and now most related efforts have been progressing toward commercialization. Scaling up the silicon-on-insulator (SOI)-based device dimensions in order to extend the operation wavelength to the short mid-infrared (MIR) range (2–4 μm) is attracting research interest, owing to the host of potential applications in lab-on-chip sensors, free space communications, and much more. Other material systems and technology platforms, including silicon-on-silicon nitride, germanium-on-silicon, germanium-on-SOI, germanium-on-silicon nitride, sapphire-on-silicon, SiGe alloy-on-silicon, and aluminum nitride-on-insulator are explored as well in order to realize low-loss waveguide devices for different MIR wavelengths. In this paper, we will comprehensively review silicon photonics for MIR applications, with regard to the state-of-the-art achievements from various device demonstrations in different material platforms by various groups. We will then introduce in detail of our institute's research and development efforts on the MIR photonic platforms as one case study. Meanwhile, we will discuss the integration schemes along with remaining challenges in devices (e.g., light source) and integration. A few application-oriented examples will be examined to illustrate the issues needing a critical solution toward the final production path (e.g., gas sensors). Finally, we will provide our assessment of the outlook of potential future research topics and engineering challenges along with opportunities.

OCIS codes: (130.0130) Integrated optics; (130.3120) Integrated optics devices; (130.6622) Subsystem integration and techniques.

https://doi.org/10.1364/PRJ.5.000417

1. INTRODUCTION

Silicon photonics, mainly referred to at the near-infrared (NIR) wavelength, have attracted great research interest in the past decade because they are a potential candidate to meet the increasing demands for high data transmission capacity in communication systems. One key driving force of silicon photonics is the fabrication compatibility with the matured CMOS technology, which has the ability to provide low-cost photonic integrated circuits (PIC) for a high volume of production. Due to the worldwide efforts fueled by researchers in the past years, silicon photonic technology working at NIR wavelength range around 1.31 and 1.55 μm for communications is now moving toward the industry from the academy.

In fact, the NIR is not only the wavelength range where silicon photonics have an impact. As shown in Fig. 1, the silicon material has the low absorption loss up to the wavelength of ~8.5 μm [1–3], which extends to the mid-infrared (MIR) region. This range covers the sensing wavelengths of a set of gases [4], including CO (~4.5 μm), CO_2 (2.65 μm, 4.2–4.3 μm), CH_4 (3.2–3.45 μm), etc. Some other toxic gases such as HF and H_2S also have the absorption peaks within this range (2.33–2.78 μm for HF, 2.5–2.75 μm for H_2S). The real-time monitoring of these gases in the environment and during the industrial process demands low cost and compact sensors. Silicon photonics stands out as a promising candidate for such application because it can provide an on-chip solution, which is cost effective and highly compact. Through the appropriate design of the optical waveguide cross-section, the evanescent field of the optical mode could overlap with the surrounding materials and consequently induce absorption loss of the light. The gas concentration can be then extracted from the output optical power detected at the end of the waveguide. Over the past few years, low-propagation-loss silicon MIR waveguides have been demonstrated by several research groups on the silicon-on-insulator (SOI) platform for the wavelength ranging from 2 to 6 μm [5–13]. In general, microring resonators (MRRs)

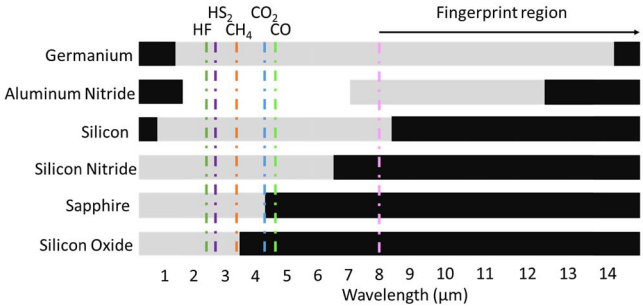

Fig. 1. Material absorption characteristic in the MIR range [1,3]. Gray region represents the optical transparency; black area denotes the high loss. Absorption peaks of some detected gases and the fingerprint region are marked.

are employed to improve the sensitivity and reduce the footprint. The light transmits in the ring with several rounds, thus essentially increasing the effective interaction lengths between the light and the detected materials. The MIR MRRs on the SOI platform were implemented and characterized in 3–5 μm [8,9,12,14]. The Vernier effect, which is constructed by MRRs for further improvement of the sensor performance at the NIR wavelength [15,16], has transferred to the MIR range by scaling up the device dimension [17,18]. The high transmission in the atmospheric window of 3–5 μm [2] also guarantees the application of silicon photonics in MIR free space communications and light detection and ranging (LIDAR) systems. Compared with the visible light and NIR waveguides, the large MIR waveguide dimension helps to improve the phase array performance used in the LIDAR system [19–23] because it alleviates the requirement of the fabrication precision as well as the phase error induced by the sidewall roughness. Moreover, the MIR lasers are safer for humans compared with their counterparts at the visible light range, as the MIR light is unable to penetrate cornea and skin tissues [24]. In addition, in the MIR range of 2–6.5 μm, the two- and three-photon absorption in silicon is negligible, permitting higher-power density transmission than at the telecom wavelengths. On the other hand, higher optical power density in the waveguides or cavities benefits nonlinearity phenomenon generation [25,26], which is utilized to explore the MIR nonlinearity devices on a silicon platform, such as the wavelength conversion [27], parametric oscillator [28,29], amplifier [30], and frequency comb generator [31]. Actually, a lot of molecules have unique identifiable absorption spectra in the MIR range of 8–20 μm [2]. It is worth to develop the on-chip photonic biosensors in this "fingerprint region." However, beyond the wavelength of 8 μm, silicon loses its competitiveness because its absorption loss drastically increases. Given the large transparency window of 2–14 μm, germanium is a suitable material for the MIR wavelength beyond 8 μm. The MIR waveguides are demonstrated in various germanium-based platforms, such as germanium-on-silicon (GOS) [32,33], germanium-on-SOI (GOI) [34–36], and germanium-on-silicon nitride (GOSN) [37]. Other platforms including silicon-on-silicon nitride (SOSN) [38], sapphire-on-silicon (SOS) [39,40], SiGe alloy-on-silicon (SGOS) [41], and aluminum nitride-on-insulator (ANOI) [42] are also explored to demonstrate the MIR photonics devices. The fabrication technology of these platforms is compatible with that of silicon photonics, while most of them use the silicon as cladding or core layers for the waveguides. Thus, in the following discussion, we consider they are silicon photonics technology in a broad sense.

With regard to the functionality, several MIR passive devices on different platforms have been demonstrated, including the fiber-chip grating couplers [5,43–46], multimode interferometers (MMIs) [6,33,47,48], Mach–Zehnder interferometers (MZIs) [49,50], MRRs [8,9,12,14,17,18,51–53], photonic crystals (PhCs) [54–56], de/multiplexers [10,57–60], polarization splitter and rotator (PSR) [61], and polarization beam splitter (PBS) [62]. These pioneering works open the way to MIR photonic integration. Besides the passive devices, the active devices, i.e., modulators, lasers, and photodetectors (PDs), are needed to compose a complete photonic system. In the reported work, the free carrier dispersion effect (FCDE) and Pockels electro-optic effect are employed to implement the modulators at short MIR wavelengths [61–67]. However, the device performance is far away from its counterparts working at NIR wavelengths. Meanwhile, because of the inherent limitation of the materials used in the aforementioned platforms, the MIR lasing and detection remain as challenges for the silicon photonics. The most promising solution for MIR laser sources is to integrate the III–V quantum well (QW) lasers and quantum cascade lasers (QCLs) [68–76] to the silicon photonics platforms. While at the detection side, the detection structures based on GeSn alloy or III–V material are monolithically integrated to the silicon substrate to build up the MIR PDs [77–80]. The detection spectral range covers the short- and middle-wave infrared.

Inspired by the success of silicon photonics at NIR, a silicon platform is considered as the most attractive solution for MIR photonics because it has potential to provide the hybrid integration system with low cost by the CMOS pilot lines. In the next sections of this paper, we will review the reported work and introduce IME's efforts on MIR photonics as follows. Section 2 presents and summarizes the researchers' elaboration upon the MIR silicon photonics devices. The material limitation and choice of integration platform are discussed in this section as well. Section 3 introduces IME's research and development efforts of MIR platforms and device library in SOI and SiN platforms. Section 4 deploys the CO_2 gas sensor as an example to demonstrate the application of the integrated MIR photonic circuit. Finally, we provide our perspective on potential future research topics and engineering challenges.

2. REVIEW OF RESEARCH FOR MIR PHOTONICS

A. Platform and MIR Waveguides

In pursuit of the optical waveguide with low propagation loss, various platforms and geometric structures were demonstrated. The reported works are summarized in Table 1. As can be seen, the SOI-based waveguides realize low loss below 2 dB/cm with the wavelength up to 4 μm by proper design of the cross-section [5–8,11,12]. With regards to the fabrication compatibility, SOI is the most preferred platform for short MIR range ($\lambda < 4$ μm). According to the low-loss MIR waveguides

Table 1. Demonstrated MIR Waveguides with Various Platforms

No.	Platform	Structure Type	Cross-Section Size (μm×μm)	Working Wavelength (μm)	Loss (dB/cm)	Pol.	Year	Ref.
1	SOI	Strip	0.9 × 0.22	2.1	0.6	TE	2012	[5]
2	SOI	Rib	0.9 × 0.34 (H_{slab} = 0.1)	2	1	TE	2016	[6]
3	SOI	Rib	2 × 2 (H_{slab} = 0.8)	3.39	0.6–0.7	TE/TM	2011	[7]
4		Rib	2 × 2 (H_{slab} = 0.8)	3.73	1.5 ± 0.2			
5	SOI	Rib	2 × 2 (H_{slab} = 0.8)	3.8	1.8 ± 0.3	TE	2012	[8]
6		Strip	1 × 0.5	3.74	4.6 ± 1.1			
7	SOI	Suspended Rib	1 × 0.34 (H_{slab} = 0.1)	2.75	3 ± 0.7	TE	2012	[9]
8	SOI	Rib	1.35 × 0.38 (H_{slab} = 0.22)	3.76	5.3	TE	2013	[10]
9		Strip	1.35 × 0.4		3.1			
10	SOI	Slot	0.65 × 0.5, (gap = 0.078 μm)	3.8	1.4 ± 0.2	Slot Mode	2015	[11]
11	SOI	Strip	4 × 2.3	3-4	<1	TE	2017	[12]
12	SOI	Strip	1.2 × 0.4	3.75	2.65 ± 0.08	TE	2017	[13]
13		Rib	1.2 × 0.4 (H_{slab} = 0.16)		1.75 ± 0.22			
14	GOS	Strip	2.9 × 2	5.8	2.5	TM	2012	[32]
15	GOS	Rib	2.7 × 2.9, (H_{slab} = 1.2)	3.8	0.6	TE	2015	[33]
16	GOI	Strip	6.5 × 0.85	3.682	~8	TE/TM	2016	[34]
17	GOI	Strip	5.5 × 0.85	3.682	~10	TE/TM	2016	[35]
18	GOI	Rib	0.6 × 0.22 (H_{slab} = 0.05)	2	14	TE	2016	[36]
19	GOSN	Strip	2 × 1	3.8	3.35 ± 0.5	TE	2016	[37]
20	SOSN	Rib	2 × 2 (H_{slab} = 0.8)	3.39	~5 ± 0.6	TE/TM	2013	[38]
21	SOS	Strip	1.8 × 0.6	4.5	4.3 ± 0.6	TE	2010	[39]
22	SOS	Strip	1 × 0.29	5.18	1.92	TE	2011	[40]
23	SGOS	Strip	3.3 × 3	4.5	1	TM	2014	[41]
24			7 × 3	7.4	2			

Pol.: Polarization.

H_{slab}: Slab thickness of the Rib waveguide, unit: μm.

demonstrated in Refs. [6,13], the SOI wafer with 340 nm top silicon and 2 μm buried oxide (BOX) is suitable for working around the wavelength of 2 μm, while the one with 400 nm top silicon and 3 μm BOX is applicable for the wavelength around 3.75 μm. Because these wafers are the commercially available products, they may become the standard platforms for the two interesting wavelengths. Beyond 4 μm, the SiO_2 becomes so lossy that other platforms are employed. Chang *et al.* first demonstrated the low-loss strip waveguide for the single TM mode at 5.8 μm on the GOS platform [32]. However, silicon has a large thermal-optic coefficient that causes the device performance sensitive to the temperature fluctuation. Therefore, GOI is adopted as the platform to fabricate the MIR waveguides because the BOX in the SOI substrate can relieve this problem as an isolation layer. Younis *et al.* recently reported the GOI waveguides at 3.682 μm, with a loss of ~8 dB/cm [34]. In their following work, the rapid thermal annealing process was used to reduce the loss [35]. Apart from a germanium-based platform, due to the wide transparent range of 1.2–6.7 μm, SiN is a promising material for MIR. The GOSN and SOSN platforms implemented by the wafer bonding provide more choices for the MIR waveguides [37,38]. However, the measured loss is not as low as expected. The authors state that the loss can be further reduced by improving the sidewall quality with advanced processes [37]. Researchers also demonstrated the MIR waveguides with SOS platform because of the low loss in sapphire below 5 μm [39,40]. But there are not obvious merits compared with other platforms, in aspects of the low loss range and the fabrication compatibility. Another attractive platform is the SiGe alloy on silicon substrate. Though controlling the ratio of silicon and germanium in the vertical direction, Brun *et al.* realized the low-loss SGOS waveguide at 4.5 and 7.4 μm [41]. From the work summarized in Table 1, one can find that the research tendency is toward longer wavelengths, and the germanium MIR waveguide is becoming a hot spot.

B. MIR Fiber-to-Chip Grating Couplers

The edge coupling scheme requires a more complicated alignment system. One typical setup is to use a CCD camera to capture the input optical mode of the fiber and judge whether it is launched into the waveguide, while an alternative is to employ a visible laser to visualize the light coupling into the waveguide. However, currently, the lack of the lensed MIR fiber limits the light coupling efficiency between the fiber and the chip. In contrary, the fiber-to-chip grating couplers provide an easier way for the light coupling. Hattasan *et al.* reported an SOI grating coupler operating in a short-wave infrared, which consists of a 220 nm thick crystalline silicon layer with a 160 nm poly-silicon overlay above [5]. The etched depth of the grating is 240 nm (80 nm into the crystal silicon layer). The coupling loss of 3.8 dB/facet at the peak wavelength of 2.1 μm with a 3 dB bandwidth of 90 nm is obtained. A suspended structure on SOI platforms is considered as one of the solutions to reduce the propagation loss caused by the BOX absorption. The focusing grating coupler for such suspended waveguides was demonstrated by Cheng *et al.* on the SOI wafer with a 340 nm top silicon layer [43]. The measured coupling efficiency at the wavelength of 2.75 μm is 24.7%, corresponding

to the coupling loss of 6.07 dB/grating. They further designed the "fishbonelike" grating couplers to improve the coupling bandwidth [44]. The uniform grating coupler with SOS platform also was experimentally demonstrated by the same group at the wavelength of 2.75 μm with the coupling efficiencies of 32.6% (4.4 dB/facet) and 11.6% (9.3 dB/facet) for TE mode and TM mode, respectively [45]. For longer wavelength at 3.8 μm, Alonso-Ramos *et al.* first demonstrated a single-etch GOS grating coupler with an inversely tapered access stage [46]. Though the coupling efficiency of 7.9% (11 dB/facet) is the highest one among the reported MIR GOS grating couplers, the coupling loss is still quite large. Among these jobs, the coupling loss of ~3–4 dB/facet around the working wavelength of 2–3 μm is close to those at the NIR range, which is efficient for the device characterization in the laboratory. But, for the practical application in products, the coupling loss needs to be further reduced. In this case, the grating couplers are not the best choice. Other coupling schemes, such as the suspended edge coupler, may be an alternative solution.

C. MIR MMIs and MZIs

The MMIs are usually utilized as the light splitters to construct the optical hybrid and modulators/switches. It is an important and basic building block in the photonic circuit. A long-wave infrared 1 × 2 MMI splitter has been demonstrated by Wei *et al.* in 2010 [47]. The device adopted the undercut structure and was characterized at the wavelength of 10.06 μm. Though the optical power at two output ports keeps an acceptable difference (~0.76 dB), the insertion loss is too large (~23 dB) for the device application and integration. In 2012, Milošević *et al.* reported the 1 × 2 MMI splitters based on submicrometer SOI strip waveguides, with the insertion loss of 3.6 ± 0.2 dB/MMI measured at 3.74 μm [48]. Followed by this work, the same group implemented the 1 × 2 MMI splitters and 2 × 2 MMI couplers with the GOS rib waveguides working at 3.8 μm. Their measured insertion loss is 0.21 ± 0.02 and 0.37± 0.07 dB/MMI, respectively. More recently, Rouifed *et al.* reported a 1 × 2 MMI splitter operating at 2 μm on the 340 nm SOI platform with an ultra-low insertion loss of 0.29 ± 0.01 dB [6]. The MZIs have been demonstrated with the SOI and GOS platforms for the wavelength of ~3.8 and ~5.3 μm [49,50]. The design approach of these commonly used components is easily transferred from those at the NIR. However, there is still a large room for improvement of their performance.

D. MIR Micro-Resonant Cavities

The versatile applications of MRRs in optical filters, routers, (de)multiplexers, and modulators make them the most thoroughly studied passive photonic devices. The efforts made on the MIR MRRs working at the MIR range are summarized in Table 2. The working wavelength of the reported SOI-based MIR MRRs range from 2.75 to 5.2 μm. An ultra-high-quality (Q)-factor of ~10^6 at the wavelength of 3.5–3.8 μm is achieved, with the extinction ratio (ER) of ~6.6 dB [8]. The ER increases with the stronger coupling between the bus and ring waveguides but at the sacrifice of the decreasing of Q-factors. As shown in Table 2, the SOI MRR demonstrated in Ref. [17] realizes a large ER around 25 dB, with a low Q-factor of 2900. The MRRs implemented with the platforms of GOS and SOS also encounter the same problems [18,51–53]. The MIR MRRs with high Q-factor and large ER are demanded for the optical signal processing. Although the MRRs-based MIR filters have been demonstrated at the working wavelength of 2.75–5.6 μm, there is no existing work demonstrating both high Q-factor and large ER. The performance of the MIR MRRs is still needed to be improved. Another type of microresonators frequently reported are PhC cavities. The typical L3 PhC cavity operating at 4–5 μm was demonstrated by Shankar *et al.* [54]. The Q-factor of 13,600 was obtained but without ER presented. In Shankar's work, because there is no coupling in and out waveguides for the demonstrated L3 PhC cavity, it is not suitable for the integration with other devices. As an improvement, Zou *et al.* demonstrated the MIR L21 PhC cavity with a coupling bus waveguide beside [56], which gives the possibility to the device as an all-pass filter. Nonetheless, as seen in Table 2, the Q-factor is decreased to 3500 due to the additional cavity loss induced by the bus waveguide coupling. Generally, compared with PhC cavities, MRRs are easier to design and have less stringent requirements of the fabrication process. Thus, MRRs are more practical for the photonic circuit integration.

E. MIR (De)multiplexers

The (de)multiplexers are widely used in the wavelength-division multiplexing (WDM) system to increase the data

Table 2. Demonstrated MIR MRRs with Various Platforms

No.	Platform	Bending Radius (μm)	Working Wavelength (μm)	Maximum Q-Factors (a.u.)	ER (dB)	FSR (nm)	Pol.	Year	Ref.
1	SOI	100	3.74	8200	4–9	4.12	TE	2012	[8]
2	SOI	40	2.75	8100	NA	NA	TE	2012	[9]
3	SOI	NA	3.5–3.8	~10^6	~6.6	NA	TE	2017	[12]
4	SOI	~17.5	5.2	2700	NA	NA	TE	2013	[14]
5			3.4	7900					
6	SOI	20, 30, 40	3.7–3.8	2900	~25	5.33	TE	2014	[17]
7	GOS	52, 142, 149	~3.8	1672	17.46	7.7	TE	2016	[18]
8	SOS	40	5.4–5.6	3000	NA	29.7	TE	2010	[51]
9	SOS	150	2.75	11400 ± 800	NA	NA	TE	2012	[52]
10	SOS	60	4.4–4.6	1.51×10^5	NA	12.4	NA	2013	[53]

FSR: free spectral range.

transmission bandwidth, the function of which is the optical signal multiplexing and routing between different channels. In particular, the (de)multiplexers are used in the spectrometers as the core elements. The arrayed waveguide gratings (AWGs) and planar concave gratings (PCGs) are the representative (de) multiplexers. The MIR AWGs based on SOI platform operating at 3.8 μm were reported by Muneeb *et al.* in 2013 [10]. The device has six output ports with insertion loss and crosstalk of −1 and −25 dB, respectively. The performance is close to the SOI AWGs at telecommunication wavelengths. The eight-port PCGs also was reported in the paper, with the insertion loss and crosstalk of 1.6 and −19.97 dB, respectively. In the same year, Malik *et al.* reported the MIR AWGs and PCGs fabricated with the GOS platform [57,58]. The devices are working at a wavelength of around 5 μm. The channel crosstalk of both devices below −20 dB is obtained for the TE mode. In 2015, Barritault *et al.* reported their AWGs based on the SGOS platform. The insertion loss of 5 dB and crosstalk < -20 dB are achieved at the wavelength of around 4.5 μm by the optimized design [59]. Thus far, the AWGs and PCGs exhibit acceptable performance at the short-wavelength infrared. Besides these two (de)multiplexers, the angled MMI (AMMI) is another (de)multiplexing device. Such a five-channel GOS-based MIR AMMI with an insertion loss of 3 dB, crosstalk of −10 dB, and channel spacing of 20 nm was demonstrated by Penades *et al.* in 2015 [60]. Though this device has a novel structure, its performance is currently not comparable with that of the AWGs and PCGs.

F. MIR Polarization Control Devices

Silicon photonics face polarization problems caused by birefringence, which results in the control of polarizations in silicon photonics devices, are of great importance. The PSR and PBS are two key components used to manipulate the polarization. A large amount of work has been done and reported on these two kinds of devices. However, most of the demonstrated devices are working at the NIR range. The PSR and PBS, intentionally designed to operate at the short-wave infrared range, were reported by Hu *et al.* in 2016 [61,62]. The proposed PSR utilize a partially etched grating-assisted coupler on the SOI platform to realize the polarization splitting and rotation in the contra direction. The device shows a conversion efficiency of 96.83% with the conversion loss of −0.97 dB at the wavelength of 2.5 μm, while maintaining the low polarization crosstalk of −21.48 dB. The PBS is proposed by using a hybrid plasmonic Y-branch on the SOI platform. The operating bandwidth is 285 nm with the center operating wavelength of 2 μm. In fact, the operating principle and design method of the MIR PSR and PBS are the same with those working at telecom wavelengths. However, to the best of our knowledge, there is no experimental demonstration of MIR, PSR, and PBS thus far. One possible reason is that the setup for polarization characterization in MIR is not as straightforward as NIR.

G. MIR Modulators

A modulator plays a key role in PICs. To date, only a few works on MIR modulators have been reported. The MIR silicon modulators operating at the wavelength of 2–3 μm based on the FCDE have been reported in [63–65]. However, the modulation speed is neither measured nor comparable with modulators working at the telecom wavelengths [66,67]. The FCDE accompanies with large absorption loss, while the wavelength is beyond 2.5 μm, which hinders the application of this scheme to longer wavelength modulation. In order to realize the modulators working at longer wavelengths, the Pockels electro-optic effect in lithium-niobate ($LiNbO_3$) and AlN are employed. Chiles and Fathpour implemented the modulators working at 3.39 μm with the silicon-on-$LiNbO_3$-based MZI [68]. Unfortunately both the modulation frequency and the efficiency are quite low. Liu *et al.* demonstrated the DC modulation at $\lambda = 2.5$ μm with the AlN waveguides [69]. The effective index change of 2×10^{-5} is obtained by applying 15 V voltage to the device. More recently, a higher-frequency (∼15 GHz) all-optical modulation in porous silicon was realized by Park *et al.* [70]. However, in terms of the construction of the NIR photonic systems, the all-optical modulation is found to be seldom used. Besides these modulation schemes, Nedeljkovic *et al.* fabricated and characterized the thermo-optic modulators on SOI that work at $\lambda = 3.8$ μm [71]. The inherent slow response, in the order of 10 kHz, of the thermo-optic effect limits such device for working in a free space communication system.

H. MIR Lasers and PDs

Silicon and germanium are inefficient material for optical light generation due to their indirect band gap. Similar to the proposed optical system prototype in the telecom wavelengths, III–V materials are utilized to fabricate the MIR lasers. The GaInAsSb/AlGaAsSb QW lasers have shown the excellent characteristics in 2–3 μm [72]. Using the quinary material (AlGaInAsSb) instead of the quaternary AlGasASb, the QW laser working wavelength could be extended to 3.4 μm [73,74]. The most promising solutions for longer MIR laser sources are the QCL. Multiwatt output power, continuous wave (CW), room temperature QCL operating in the wavelength ranging from 3 to 20 μm have been demonstrated during the past two decades [75–77]. More recently, some pioneer work of the MIR laser integration with the waveguides also have been reported [78–80]. In both the on-chip sensors and the LIDAR systems, the MIR PDs are the necessary components to receive the optical signals. At the short-wave infrared range, the GeSn alloy attracts a lot of interest to build up the detectors due to its widely tunable bandgap. The GeSn MIR PDs fabricated on silicon substrate were reported in Refs. [81,82]. The devices can work at the wavelength up to 2.3 μm with a responsivity of ∼0.1 A/W. Wang *et al.* demonstrated the PbTe-based PDs at the wavelengths of 3.5 and 3.7 μm where the entire detector structure was directly deposited onto a silicon substrate [83,84]. Wu *et al.* recently reported the monolithically integrated InAs/GaAs quantum-dot MIR PDs on silicon substrate [85]. The detection range of the device is up to ∼8 μm at 80 K. This work proves that the direct integration of III–V PDs to the silicon photonics circuit is feasible. However, the low cost and high yield approach to integrate these III–V components, including the lasers and PDs, with silicon photonic platform remains a

challenge. The integration method demonstrated at telecom wavelengths may provide an example for the MIR range [86].

3. MIR PLATFORMS AND DEVICE LIBRARY IN IME

IME has been spearheading the R&D on silicon photonics over the past decade with various silicon photonics devices, products, and platform building. It is natural for us now to extend our work to the MIR range. The preliminary effort is to develop the appropriate platforms for the MIR passive device design and fabrication. In this section, we will introduce the basic MIR photonic components demonstrated in IME on the SOI and SNOI platform. The devices, including the strip/rib waveguides, bending waveguides, directional couplers (DCs), and MRRs, were characterized at the short-wave infrared of ~3.7 and ~2 μm, respectively. The research efforts of ANOI based devices are in progress, and it is expected to have some exciting demonstrations in the near future.

A. SOI Platform at 3.8 μm

The SOI device fabrication starts from a commercially available 8-in. SOI wafer with 220 nm top silicon layer and 3 μm BOX layer. Blanket silicon epitaxy is performed to increase the top silicon thickness to 400 nm. SiO_2 is deposited as the hard mask for fine structure definition. The device is patterned by deep ultraviolet (DUV) photolithography followed by a two-step silicon reactive ion etching (RIE) to define the waveguide devices. The 3 μm cladding SiO_2 is deposited using plasma-enhanced chemical vapor deposition (PECVD). Finally, a deep trench is formed for butt fiber coupling.

The optical and scanning electron microscope (SEM) images of the fabricated SOI devices are shown in Figs. 2(a)–2(i). To ensure a good optical mode confinement in the silicon core and maintain the single-mode condition at 3.70 μm for strip waveguide and 3.75 μm for rib waveguide, the SOI strip waveguide is designed with a cross-section of $w \times h = 1.2\ \mu\text{m} \times 0.4\ \mu\text{m}$, while the rib waveguide is 1.2 μm in width and has 0.24 μm etch depth. The SEM image of them are shown in Figs. 2(e) and 2(f), respectively. The light is coupled from a ZrF_4 fiber to a waveguide taper tip with 0.2 μm width [Fig. 2(d)] and adiabatically tapered to the waveguide through 200 μm tapering length. Figure 3 presents the loss of an SOI waveguide measured by the cutback method. The measured propagation loss at 3.75 μm of the strip waveguide and rib waveguide is plotted in Figs. 3(a) and 3(c). The linear fitting results indicate the loss of the two type of waveguides is 2.65 ± 0.08 and 1.75 ± 0.22 dB/cm, respectively, which is comparable with the reported best data. We also study the bending loss of bends with different bending radius. As shown in Fig. 3(b), the bending loss gradually decreases from 0.054 to 0.008 dB/90°, as the bending radius increases from 5 to 25 μm. The reduction of bending loss could be attributed to smaller mode mismatch, as the light travels from a straight to bend waveguide and lower radiation loss for a bend with a larger bending radius.

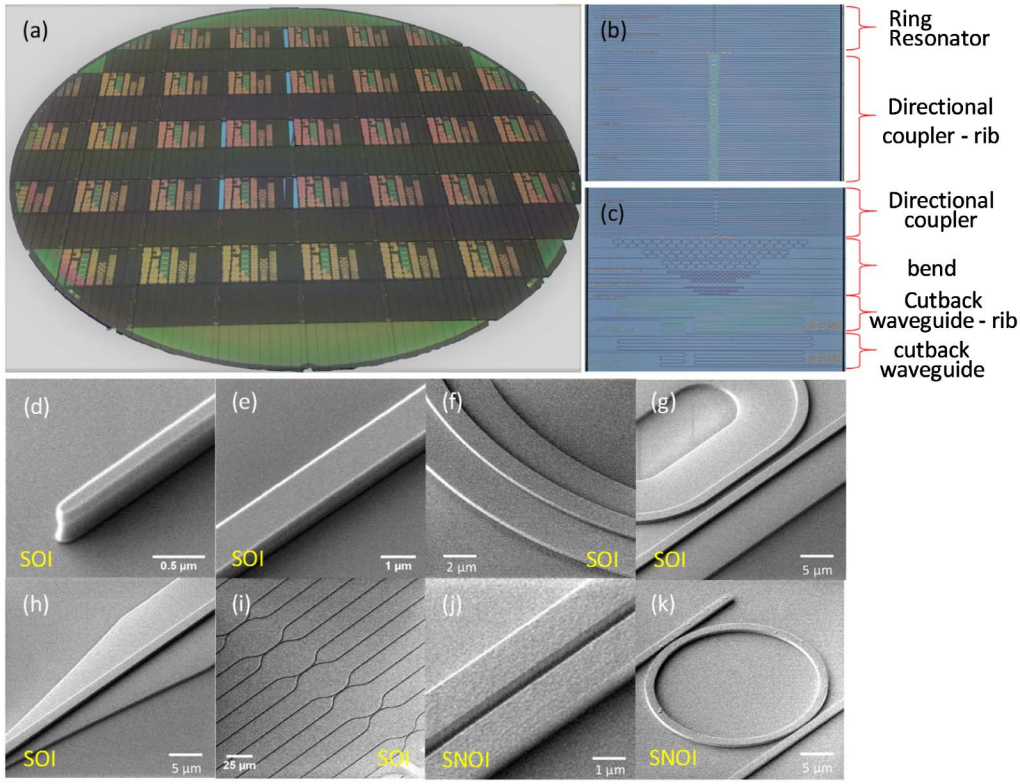

Fig. 2. (a) Fabricated 8-in. silicon wafer with MIR devices after wafer dicing for characterization. (b) SOI strip ring resonators and rib DCs. (c) SOI strip DCs, bends, waveguides, and rib waveguides. (d)–(k) SEM images of the fabricated devices. (d) SOI waveguide taper tip. (e) SOI strip waveguide. (f) SOI rib waveguide. (g) SOI rib DC. (h) SOI strip to rib converter. (i) SOI strip DC array. (j) SNOI DC. (k) SNOI add–drop ring resonator.

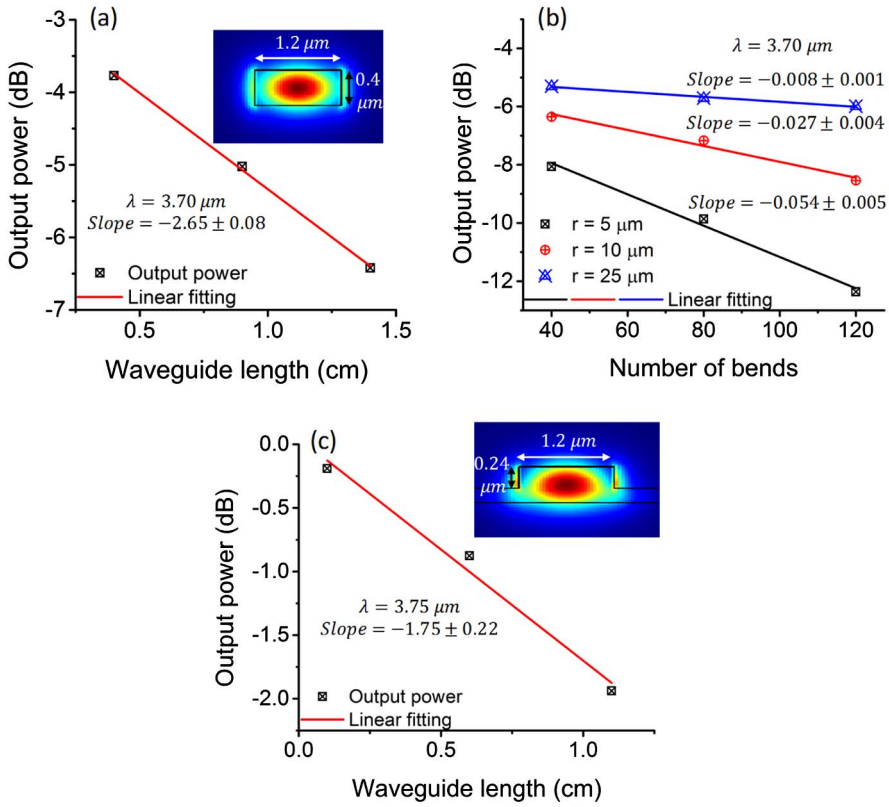

Fig. 3. Loss characterization of SOI waveguide. (a) Propagation loss of SOI strip waveguide. (b) Bending loss of SOI strip waveguide. (c) Propagation loss of SOI rib waveguide. Insets in (a) and (c) show the corresponding mode field simulated by the commercial software Lumerical FDTD.

Based on the good propagation and bending loss result, we fabricated an SOI strip [Fig. 2(i)] and rib [Fig. 2(g)] DCs with gap $g = 500$ nm and varying coupling lengths L_c. The coupled mode theory (CMT) was applied to analyze the DCs enabled by evanescent wave coupling in previous studies. The coupling in the S bend region, which brings two far-apart waveguides close to allow for evanescent wave coupling, was considered negligible. Though this assumption might be valid in NIR, in MIR the optical mode is less confined, which will cause significant coupling in the S bend region. Due to this fact, we slightly modify the equation obtained previously by the CMT by adding an initial phase $\varnothing_0$ to take coupling in the S bend region into account [13]:

$$\frac{T}{I} = t^2 = \cos^2\left(\frac{\pi}{2}\frac{L_c}{L_\pi} + \varnothing_0\right), \tag{1}$$

$$\frac{X}{I} = K^2 = \sin^2\left(\frac{\pi}{2}\frac{L_c}{L_\pi} + \varnothing_0\right), \tag{2}$$

$$Y = \arctan\left(\sqrt{X/T}\right) = \left(\frac{\pi}{2L_\pi}\right)L_c + \varnothing_0. \tag{3}$$

In Eqs. (1) and (2), T is the power transmitted through the waveguide. X is the power coupled evanescently to the neighboring waveguide. $I = X + T$ is the total power in the DCs. t is the power transmission coefficient. K is the power coupling coefficient. L_c is the coupling length of the straight coupling region. L_π is the straight length to achieve π phase shift. $\varnothing_0$ is the initial phase introduced by S bends. Equation (3) is derived from Eqs. (1) and (2). By linear fitting Y with respect to L_c, L_π and $\varnothing_0$ can be extracted. The characterization results of SOI strip and rib DCs are shown in Figs. 4(a) and 4(c). The 50% power splitting ratio is achieved at the coupling lengths of 21 and 8 μm, respectively. The sine squared fitting suggested by Eqs. (1) and (2) results in an adjusted R-square value of 0.997, showing the consistency between the data and our proposed model. Linear fitting results of Y with respect to L_c suggested by Eq. (3) are shown in Figs. 4(b) and 4(d) as insets. The extracted slope and intercept, which presents $\frac{\pi}{2L_\pi}$ and $\varnothing_0$, respectively, are substituted into Eq. (2) to obtain the power coupling coefficient K. Figure 4(d) reveals a K value of ~0.4 at $L_c = 0$, corresponding to the 16% coupling caused by the S bend region. This significant amount of coupling demonstrates that including $\varnothing_0$ term in our proposed model is significant.

We also fabricate SOI strip racetrack MRRs with different coupling lengths and gaps. Figure 5(a) shows the transmission spectrum of the MRRs with the bending radius of 5 μm and the gap of 500 nm. The coupling length between the ring and the bus waveguide is 5 μm. The red solid dot is the detected optical power by the power meter. Limited by the laser scanning step of 0.5 nm, the CMT and transfer matrix method are used to fit the measured data. The blue line is the fitted transmission spectrum. The Q-factor of ~5900, ER of ~6.84, and free spectral range (FSR) of ~85 nm are extracted from the zoom in the

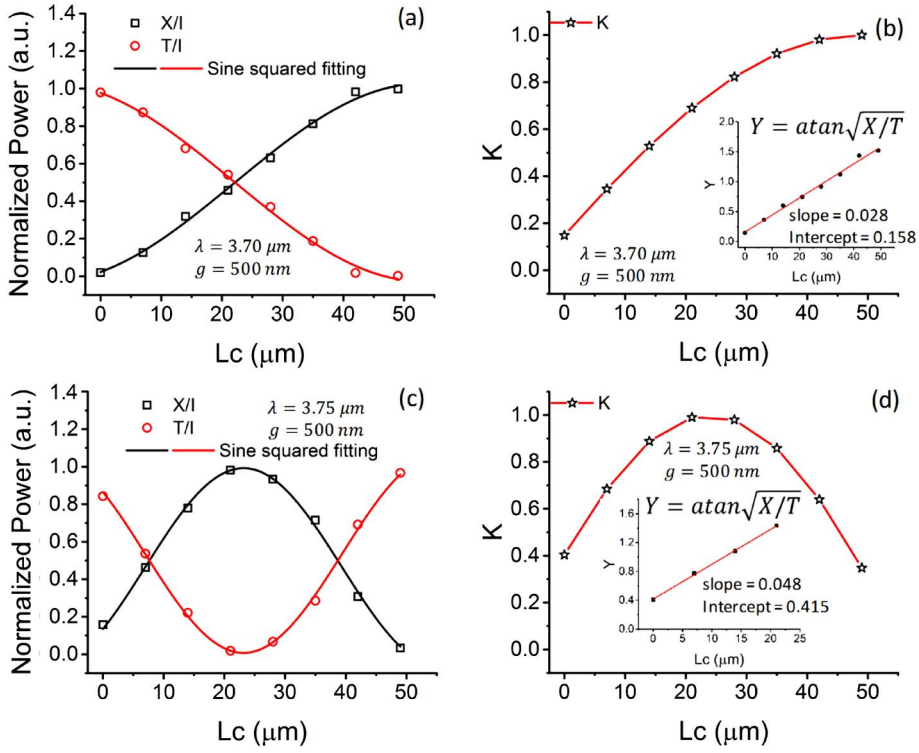

Fig. 4. Characterization of SOI strip and rib DCs. (a) and (c) Self-normalized transmitted and coupled power of (a) strip and (c) rib DCs. Solid lines show sine squared fitting of the data with adjusted R-square of 0.997. (b) and (d) Power coupling coefficient K of (b) strip and (d) rib DCs. Insets show the linear fitting of Y with respect to L_c with the extracted parameters L_π and $\varnothing_0$.

spectrum shown in Fig. 5(b). The theoretical spectra for both MRRs fit the experimental data very well, where the group index is obtained by the Lumerical FDTD simulation. The dispersion relation of the effective index is expressed as $n_{\text{eff}}(\lambda) = (-0.4839 \times 10^6) * \lambda + 3.9666$. The coupling coefficient and round-trip loss are 0.225 and 0.981, respectively. The transmission spectrum of a rib racetrack MRRs is shown in Figs. 5(c) and 5(d), from which we see that the Q-factor of ~4500, ER of ~5.29, and FSR of ~67.84 nm. By the optimized physical parameters, the MRRs can be designed working close or even at the critical coupling condition to realize a high Q and a large ER simultaneously.

B. SNOI Platform at 2 μm

The SNOI device fabrication starts from a commercially available 8-inch silicon wafer. A 4 μm thick SiO_2 is first deposited by PECVD as the insulating layer. 400 nm silicon nitride (Si_3N_4) is then deposited by PECVD as the device layer. The following fabrication steps for the device formation are similar to those of SOI devices, as mentioned above.

The SNOI strip waveguide is designed with a cross-section of $w \times h = 1$ μm × 0.6 μm for application at 2 μm [Fig. 6(a) inset]. The light is coupled from a ZrF_4 fiber to a waveguide taper tip with 0.3 μm width and adiabatically tapered to the waveguide through 200 μm tapering length. The loss characterization result of SNOI waveguide is shown in Fig. 6. The propagation loss of our SNOI waveguide is 2.52 ± 0.10 dB/cm at 2 μm. Figure 6(b) demonstrates the bending loss of an SNOI bend with various bending radius. For a 10 μm radius bend, the output power is below −40 dBm, which is the threshold of the PD. Hence, the 10 μm radius bend is too lossy for light transmission. For 10 and 50 μm radius bend, the bending loss is 0.147 ± 0.006 and 0.029 ± 0.002 dB/cm, respectively. Thus, for SNOI devices for MIR application, the bend radius should be large enough in order for less propagation loss.

The SNOI strip MRRs are fabricated as well [Fig. 2(k)]. Figure 7 shows the characterization result of our SNOI strip ring resonator with the radius of 20 μm and gap of 550 nm. As seen from the zoom-in spectrum in Fig. 7(b), a higher ER of 11.36 dB is obtained, but at the price of a low Q-factor around 3200. The trade-off between the Q and ER can be achieved through appropriate design of the MRRs dimension.

4. APPLICATIONS FOR MIR PHOTONIC SENSORS

As mentioned in Section 1, the MIR photonics has the potential to realize the portable, cost-effective, and mass-produced integrated systems for applications such as on-chip sensors, free space communications, LIDAR, and thermal imaging. In this section, we will discuss the CO_2 gas sensors as an example to illustrate the applications of the integrated MIR photonics. An on-chip gas sensor is usually composed of three parts: the laser diode, analyte interaction component (absorption of the optical evanescent field), and PD. The hybrid integration technology for MIR laser and PDs are discussed in Section 2.G, whereas here we focus on the analyte interaction part.

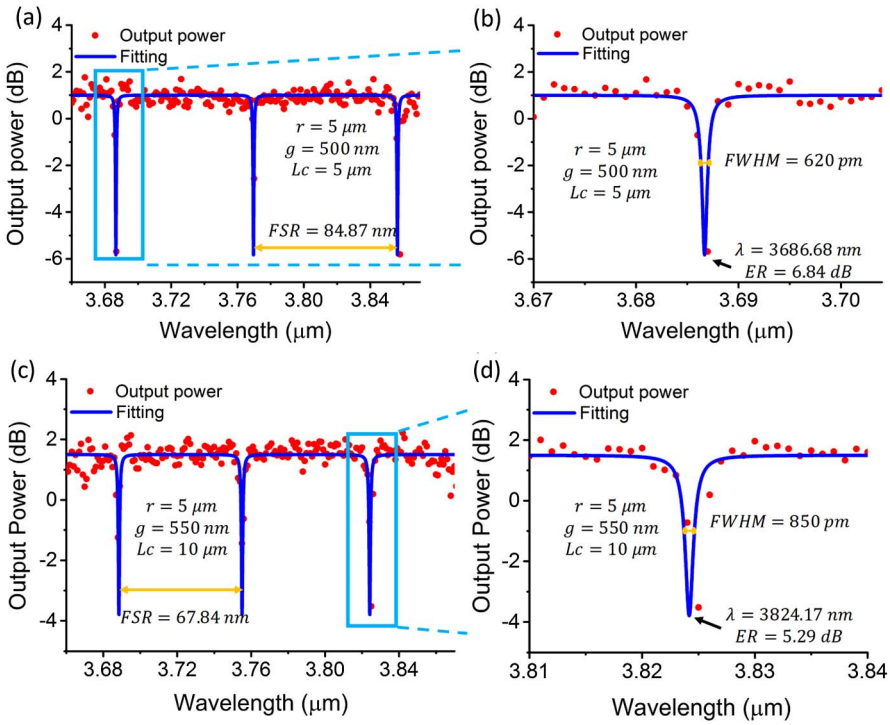

Fig. 5. Characterization of SOI strip racetrack resonators. Red dots present measurement data, while the blue solid lines show fitting results. (a) and (c) Transmission spectra of the racetrack resonator with (a) $r = 5$ μm, $g = 500$ nm, and $L_c = 50$ μm, (c) $r = 5$ μm, $g = 550$ nm, and $L_c = 10$ μm. (b) and (d) Zoom-in of a particular resonating wavelength at ~3687 nm in (a) and ~3824 nm in (c) as indicated by the navy blue square box.

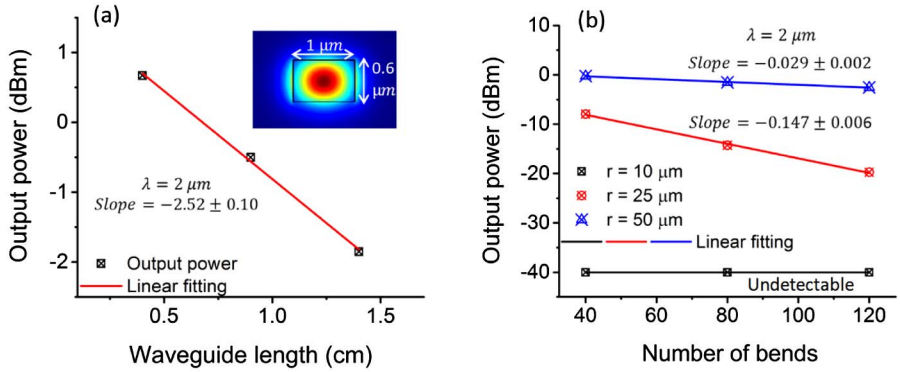

Fig. 6. Loss characterization of SNOI waveguide. (a) Propagation loss of SNOI strip waveguide. (b) Bending loss of SNOI strip waveguide. Inset in (a) shows the mode field simulated by Lumerical.

The detection limit and sensitivity are the most important performance metrics in the gas sensor. In order to enhance these metrics, choosing the high absorption wavelength and increasing the effective interaction optical path are the commonly used methods. In the MIR region, the absorption coefficient of the pure concentration CO_2 is larger than 80 cm^{-1} at the MIR wavelength around 4.3 μm [87]. This strong absorption gives the ability to achieve the high sensitivity sensing of CO_2 with the MIR photonics. On the other hand, the approaches to increase the effective interaction optical path can be classified into two categories. One is to design the true optical length structures such as the spiral waveguides [88]. The other is to use the resonator, such as MRRs, to guide the light with multiple passes [89].

A concept of the MIR photonics-based CO_2 gas sensor is shown in Fig. 8(a). A polydimethylsiloxane (PDMS) gas chamber with the inlet/outlet is adhered to the optical spiral waveguide area to form the analyte interaction region. The waveguide cross-section is designed with a confinement factor Γ. The optical transmission power can be evaluated by the Beer–Lambert Law [88]:

$$T = \exp(-\alpha_g C \Gamma L), \tag{4}$$

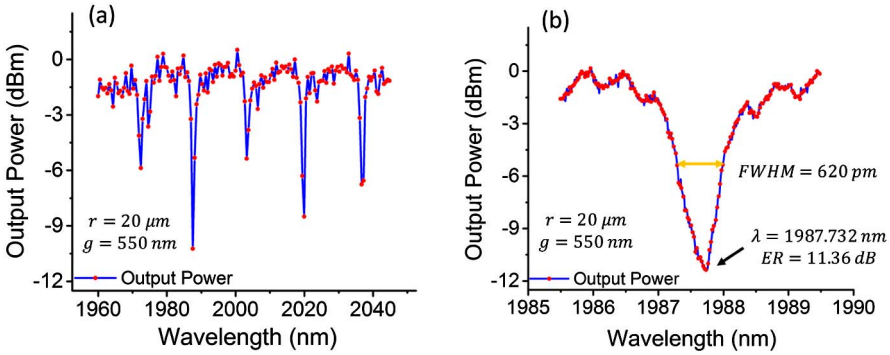

Fig. 7. Characterization of the SNOI strip ring resonator with radius of 20 μm and coupling gap of 550 nm. Transmission spectrum of the ring resonator (a) from 1960 to 2045 nm with scanning step of 0.54 nm (b) around the resonance of 1988 nm with scanning step of 0.011 nm.

where α_g is the absorption coefficient of 100% CO_2 (partial pressure 1 atm), C is the volume concentration of the CO_2, and L is the waveguide length, which interacts to the analyte gas. Assuming Γ is 0.6 and the absorption coefficient is linearly proportional to the gas concentration (80 cm^{-1} for 100% CO_2). The calculated power variation as the function of the CO_2 concentration is shown in Fig. 8(b). The detected CO_2 concentration is around 500 ppm for a 50% optical power variation in a 30 or 40 cm spiral waveguide, while for the same power variation, the detection concentration is 1200 ppm for a 10 cm long spiral waveguide. Assuming the optical power launched into the spiral waveguide is 0 dBm, the optical propagation loss in the waveguide is ~1.5 dB/cm, and the detection limit of the PDs is −90 dBm, the spiral waveguide of 40 cm is feasible to undergo a 30 dB optical power variation (100%–0.1%) for gas sensor. As shown in Fig. 8(b), for the 40 cm long spiral waveguide, the detection concentration reaches 110 ppm with a 20% (~0.97 dB) power variation. The sensitivity near 200 ppm is calculated as ~8.4×10^{-3} dB/ppm from Fig. 8(b). It increases as the CO_2 concentration becomes lower, which indicates that the sensor has the detection limit below 20 ppm, as such CO_2 concentration change would induce a readable optical power variation of ~0.17 dB at the detector. If the propagation loss can be further reduced and a longer spiral waveguide is used, the detection limit can be improved to be below 10 ppm.

In the MRRs, the light with the resonant wavelength propagates for several rounds. This allows the MRRs to provide an effective long path for the optical evanescent field to interact with the analyte gases. Figure 8(c) shows the configuration of MRRs absorption enhanced gas sensor. The gas absorption will induce the change of resonance line shape in transmission

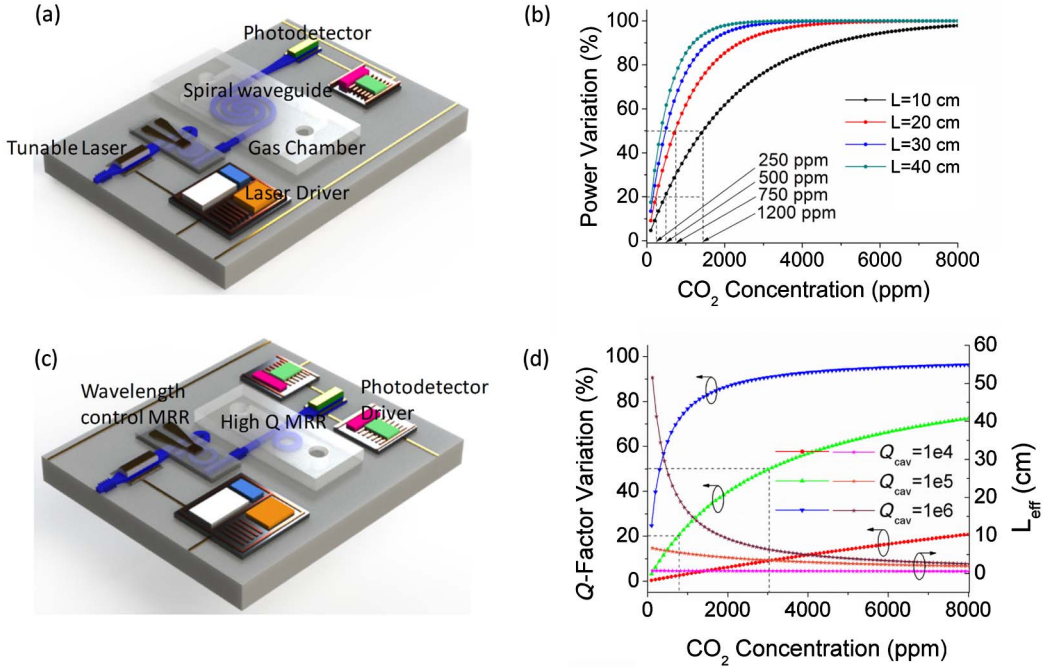

Fig. 8. CO_2 gas sensors based on MIR photonics. Sensor configuration with the (a) spiral waveguide and (c) MRR. (b) Detected optical power variation versus CO_2 concentration of the sensor shown in (a). (d) Q-factor variation and effective gas interaction length varying with CO_2 concentration of the sensor shown in (b).

spectrum. Through the inspection of the line shape change, i.e., monitoring the change of Q-factor or ER, the concentration change of analyte gas can be measured [89]. In terms of the CMT, the Q-factor of the MRR is expressed as [90]

$$\frac{1}{Q}=\frac{1}{Q_i}+\frac{1}{Q_c}+\frac{1}{Q_g}=\frac{1}{Q_{\text{cav}}}+\frac{1}{Q_g}, \tag{5}$$

where Q_i is the intrinsic quality factor of the of the MRR, while Q_c is the coupling quality factor between the bus and the ring waveguide. Q_{cav} is the combination quality factor of Q_i and Q_c. The analyte gas absorption loss contributes the quality factor of Q_g, which is descripted as

$$Q_g=\omega\tau_p=\frac{2\pi}{\lambda\Gamma C\alpha_g}, \tag{6}$$

where ω, λ, and τ_p are the angular frequency, vacuum wavelength, and photon life time of the light resonant in the MRR. In terms of Eq. (5), when Q_{cav} is comparable or larger than Q_g, the considerable influence of the gas absorption on the total Q will be observed. The relationship between the Q-factor variation and the CO_2 concentration is plotted in Fig. 8(d). As can be seen, for the MRR with an original Q-factor of 10^5, taking the CO_2 (concentration of ~800 ppm) absorption into account, the 20% variation of Q-factor is inspected. The same Q variation of the MMR with Q-factor of 10^4 can only detect the CO_2 concentration of ~8000 ppm. The sensitivity near 200 ppm is around 3.43×10^{-4}/ppm for the MRR with Q of 10^5. Assuming that 2% variation of Q can be observed in the detection analysis, the estimated detection limit of such MRR is around 58 ppm. Obviously, the MMRs with higher Q have the potential capability to detect the CO_2 with concentration below 10 ppm. However, it is a challenge to demonstrate the MRR with Q over $\sim10^6$ on silicon photonic platform. In fact, the high Q MRR increases the effective interaction length between the optical evanescent fields and the detection gas, which can be calculated by

$$L_{\text{eff}}=c\tau_p=\frac{cQ}{\omega}=\frac{\lambda Q}{2\pi}, \tag{7}$$

where c is the light speed in the vacuum. The L_{eff} varying with the CO_2 concentration is shown in Fig. 8(d) as well. The effective optical transmission length under the 200 ppm CO_2 for the MRR with original Q of 10^5 is around 6.42 cm. Assuming that the MRR radius is in the order of several 10s μm, the footprint is <0.031 mm^2. In contrast, realizing the comparable performance, the spiral waveguide composed of multiple bend waveguides with radius ranging from 10 to 1000 μm is needed, the footprint of which could be as large as ~100 mm^2. The footprint of MRR is thus 1000 times smaller, while the detection limit could be comparable. However, one of the disadvantages of the MRR-based gas sensor is the inevitable use of the wavelength scanning method. To adopt the wavelength scanning method, the sensor must be equipped with a tunable MIR laser in order to obtain optical transmission spectrum change to calculate the analyte gas concentration. As an attempt to eliminate the utilization of a tunable laser, an electrical tracing assisted MRR sensing system could be adopted [91]. In pursuit of improving the detection limit, other complicated MIR photonic devices are innovated. One of them is the photoacoustic (PA) gas sensor [92]. The detected gas molecules in the PA sensor chamber are excited to a higher-energy state by absorbing the MIR photon (injected from an MIR waveguide) energy. Then it is relaxed to the ground state by releasing the energy through collision with other molecules. An efficient MEMS microphone is used to detect the acoustic wave generated in this process. This type of sensor can achieve a detection limit below 10 ppm yet through a more complicated fabrication process with multiple bonding wafers.

5. SUMMARY AND FUTURE OUTLOOK

The MIR photonics is becoming a hot research topic. We reviewed in this paper the recent R&D efforts of the silicon-based MIR photonics. Up to date, the platforms of SOI, GOS, GOI, GOSN, and SOS have been explored for the MIR passive device demonstration. The waveguides with different structures are implemented on these platforms, covering the wavelength range from 2 to 7.4 μm. The main achievements of the passive MIR photonic devices, including the grating couplers, MMIs, MZIs, MRRs, PhC cavities, and (de)multiplexers, are summarized in Section 2, as well as the active devices of MIR modulators, laser sources, and PDs. We also reviewed IME's research and development efforts on the MIR photonic platforms. The basic passive MIR components with an SOI and SNOI platform are fabricated and characterized at the wavelengths of 3.8 and 2 μm. The MIR QCL laser sources, PDs, and relevant integration technology are under design and experiments. The discussion of the CO_2 gas sensors illustrated one of the applications of the integrated MIR photonic system. Theoretical analysis indicates that the detection limit of 20 ppm can be achieved for the 40 cm spiral waveguide with the propagation loss less than 1.5 dB/cm. For the MRR-based CO_2 gas sensor, the Q-factor is required to be larger than 10^5 to obtain a detection limit below 60 ppm. The detection limit below 10 ppm is possible by utilizing longer spiral waveguide or MRR with higher Q.

Although MIR photonics has attracted increasing research interests, there are still many areas requiring further exploitation, including:

1) Platform development for low-loss waveguide beyond 7.4 μm. The MIR waveguides with propagation loss <3 dB/cm have been demonstrated in different platforms with wavelengths of less than 7.4 μm. However, as of now, there are very limited demonstrations of a silicon photonics platform for low-loss waveguides beyond the 7.4 μm wavelength range, especially for the long-wavelength fingerprint region.

2) Performance improvement of MIR optical filters. Although MRRs-based MIR filters have been demonstrated at the working wavelength of 2.75–5.6 μm, as far as we know, there is no demonstration that achieves both high Q-factor and large ER simultaneously, which is demanded for the signal processing. Moreover, there lacks demonstration of MIR optical filters that work at the middle- and long-wavelength range beyond 5.6 μm.

3) The development of MIR modulators. The FCDE-based electrical-driven modulators are reported only at a short wavelength of 2–3 μm, and with less impressive device

performance compared with their counterparts at the telecom wavelengths. The low-loss, high-speed, and power-efficient MIR modulators have not yet been implemented. Besides, the free carrier absorption increases significantly with wavelengths beyond 2.5 μm. Thus, new optical modulation schemes and corresponding structures are highly desired.

4) Integration of the MIR lasers and PDs to the photonic circuits. So far, most of the research efforts are made on the MIR platform development and discrete device demonstration. To the best of our knowledge, there is no report on an MIR photonic circuit that integrates laser sources and PDs with the passive MIR photonic devices. This is partially due to the incomplete device library of MIR photonics as well as the immature integration scheme of MIR lasers and detectors. Exploiting the integration technology is essential for the realization of the portable and cost-effective MIR photonic system to fulfill the applications of lab-on-chip sensors, free space communications, etc.

Acknowledgment. We thank Ms Xin Guo and Prof. Hong Wang from School of Electrical & Electronic Engineering, Nanyang Technological University for their great support on the device characterization.

REFERENCES

1. R. Soref, "Mid-infrared photonics in silicon and germanium," Nat. Photonics **4**, 495–497 (2010).
2. R. Shankar and M. Lončar, "Silicon photonic devices for mid-infrared applications," Nanophotonics **3**, 329–341 (2014).
3. E. D. Palik, *Handbook of Optical Constants of Solids* (Academic, 1998), Vol. **1**.
4. V. M. Lavchiev and B. Jakoby, "Photonics in the mid-infrared: challenges in single-chip integration and absorption sensing," IEEE J. Sel. Top. Quantum Electron. **23**, 8200612 (2017).
5. N. Hattasan, B. Kuyken, F. Leo, E. M. P. Ryckeboer, D. Vermeulen, and G. Roelkens, "High-efficiency SOI fiber-to-chip grating couplers and low-loss waveguides for the short-wave infrared," IEEE Photon. Technol. Lett. **24**, 1536–1538 (2012).
6. M.-S. Rouifed, C. G. Littlejohns, G. X. Tina, Q. Haodong, T. Hu, Z. Zhang, C. Liu, G. T. Reed, and H. Wang, "Low loss SOI waveguides and MMIs at the MIR wavelength of 2 μm," IEEE Photon. Technol. Lett. **28**, 2827–2829 (2016).
7. G. Z. Mashanovich, M. M. Milošević, M. Nedeljkovic, N. Owens, B. Xiong, E. J. Teo, and Y. Hu, "Low loss silicon waveguides for the mid-infrared," Opt. Express **19**, 7112–7119 (2011).
8. M. M. Milosević, M. Nedeljkovic, T. M. B. Masaud, E. Jaberansary, H. M. H. Chong, N. G. Emerson, G. T. Reed, and G. Z. Ashanovich, "Silicon waveguides and devices for the mid-infrared," Appl. Phys. Lett. **101**, 121105 (2012).
9. Z. Cheng, X. Chen, C. Y. Wong, K. Xu, and H. K. Tsang, "Mid-infrared suspended membrane waveguide and ring resonator on silicon-on-insulator," IEEE Photon. J. **4**, 1510–1519 (2012).
10. M. Muneeb, X. Chen, P. Verheyen, G. Lepage, S. Pathak, E. Ryckeboer, A. Malik, B. Kuyken, M. Nedeljkovic, J. V. Campenhout, G. Z. Mashanovich, and G. Roelkens, "Demonstration of silicon-on-insulator mid-infrared spectrometers operating at 3.8 μm," Opt. Express **21**, 11659–11669 (2013).
11. J. S. Penadés, A. Z. Khokhar, M. Nedeljkovic, and G. Z. Mashanovich, "Low-loss mid-infrared SOI slot waveguides," IEEE Photon. Technol. Lett. **27**, 1197–1199 (2015).
12. S. A. Miller, M. Yu, X. Ji, A. G. Griffith, J. Cardenas, A. L. Gaeta, and M. Lipson, "Low-loss silicon platform for broadband mid-infrared photonics," Optica **4**, 707–712 (2017).
13. B. Dong, X. Guo, C. P. Ho, B. Li, H. Wang, C. Lee, X. Luo, and G.-Q. Lo, "Silicon-on-insulator waveguide devices for broadband mid-infrared photonics," IEEE Photon. J. **9**, 4501410 (2017).
14. Y. Xia, C. Qiu, X. Zhang, W. Gao, J. Shu, and Q. Xu, "Suspended Si ring resonator for mid-IR application," Opt. Lett. **38**, 1122–1124 (2013).
15. L. Qin, L. Wang, M. Li, and J. He, "Optical sensor based on Vernier-cascade of a ring resonator and an echelle diffraction grating," IEEE Photon. Technol. Lett. **24**, 954–956 (2012).
16. X. Jiang, Y. Chen, F. Yu, L. Tang, M. Li, and J. He, "High-sensitivity optical biosensor based on cascaded Mach-Zehnder interferometer and ring resonator using Vernier effect," Opt. Lett. **39**, 6363–6366 (2014).
17. B. Troia, A. Z. Khokhar, M. Nedeljkovic, J. S. Penades, V. M. N. Passaro, and G. Z. Mashanovich, "Cascade-coupled racetrack resonators based on the Vernier effect in the mid-infrared," Opt. Express **22**, 23990–24003 (2014).
18. B. Troia, J. S. Penades, A. Z. Khokhar, M. Nedeljkovic, C. Alonso-Ramos, V. M. N. Passaro, and G. Z. Mashanovich, "Germanium-on-silicon Vernier-effect photonic microcavities for the mid-infrared," Opt. Lett. **41**, 610–613 (2016).
19. J. K. Doylend, M. J. R. Heck, J. T. Bovington, J. D. Peters, L. A. Coldren, and J. E. Bowers, "Two-dimensional free space beam steering with an optical phased array on silicon-on-insulator," Opt. Express **19**, 21595–21604 (2011).
20. J. Sun, E. Timurdogan, A. Yaacobi, E. S. Hosseini, and M. R. Watts, "Large-scale nanophotonic phased array," Nature **493**, 195–199 (2013).
21. D. Kwong, A. Hosseini, J. Covey, Y. Zhang, X. Xu, H. Subbaraman, and R. T. Chen, "On-chip silicon optical phased array for two-dimensional beam steering," Opt. Lett. **39**, 941–944 (2014).
22. A. Yaacobi, J. Sun, M. Moresco, G. Leake, D. Coolbaugh, and M. R. Watts, "Integrated phased array for wide-angle beam steering," Opt. Lett. **39**, 4575–4578 (2014).
23. C. V. Poulton, M. J. Byrd, M. Raval, Z. Su, N. Li, E. Timurdogan, D. Coolbaugh, D. Vermeulen, and M. R. Watts, "Large-scale silicon nitride nanophotonic phased arrays at infrared and visible wavelengths," Opt. Lett. **42**, 21–24 (2017).
24. M. Pfennigbauer and A. Ullrich, "Multi-wavelength airborne laser scanning," in *Proceedings of the International Lidar Mapping Forum, ILMF*, New Orleans, Louisiana, 2011.
25. B. Jalali, "Silicon photonics: nonlinear optics in the mid-infrared," Nat. Photonics **4**, 506–508 (2010).
26. S. Zlatanovic, J. S. Park, S. Moro, J. M. C. Boggio, I. B. Divliansky, N. Alic, S. Mookherje, and S. Ra, "Mid-infrared wavelength conversion in silicon waveguides using ultracompact telecom-band-derived pump source," Nat. Photonics **4**, 561–564 (2010).
27. B. Kuyken, P. Verheyen, P. Tannouri, X. Liu, J. Van Campenhout, R. Baets, W. M. J. Green, and G. Roelkens, "Generation of 3.6 μm radiation and telecom-band amplification by four-wave mixing in a silicon waveguide with normal group velocity dispersion," Opt. Lett. **39**, 1349–1352 (2014).
28. B. Kuyken, X. Liu, G. Roelkens, R. Baets, R. M. Osgood, and W. M. J. Green, "50 dB parametric on-chip gain in silicon photonic wires," Opt. Lett. **36**, 4401–4403 (2011).
29. B. Kuyken, X. Liu, R. M. Osgood, Jr., R. Baets, G. Roelkens, and W. M. J. Green, "A silicon-based widely tunable short-wave infrared optical parametric oscillator," Opt. Express **21**, 5931–5940 (2013).
30. X. Liu, R. M. Osgood, Jr., Y. A. Vlasov, and W. M. J. Green, "Mid-infrared optical parametric amplifier using silicon nanophotonic waveguides," Nat. Photonics **4**, 557–560 (2010).
31. A. G. Griffith, R. K. W. Lau, J. Cardenas, Y. Okawachi, A. Mohanty, R. Fain, Y. H. D. Lee, M. Yu, C. T. Phare, C. B. Poitras, A. L. Gaeta, and M. Lipson, "Silicon-chip mid-infrared frequency comb generation," Nat. Commun. **6**, 6299 (2015).
32. Y. Chang, V. Paeder, L. Hvozdara, J. Hartmann, and H. P. Herzig, "Low-loss germanium strip waveguides on silicon for the mid-infrared," Opt. Lett. **37**, 2883–2885 (2012).
33. M. Nedeljkovic, J. S. Penadés, C. J. Mitchell, A. Z. Khokhar, S. Stankovíc, T. D. Bucio, C. G. Littlejohns, F. Y. Gardes, and G. Z. Mashanovich, "Surface-grating-coupled low-loss Ge-on-Si rib waveguides and multimode interferometers," IEEE Photon. Technol. Lett. **27**, 1040–1043 (2015).

34. U. Younis, S. K. Vanga, A. E. Lim, P. G. Lo, A. A. Bettiol, and K. Ang, "Germanium-on-SOI waveguides for mid-infrared wavelengths," Opt. Express **24**, 11987–11993 (2016).
35. U. Younis, A. E. Lim, P. G. Lo, A. A. Bettiol, and K. Ang, "Propagation loss improvement in Ge-on-SOI mid-infrared waveguides using rapid thermal annealing," IEEE Photon. Technol. Lett. **28**, 2447–2450 (2016).
36. J. Kang, M. Takenaka, and S. Takagi, "Novel Ge waveguide platform on Ge-on-insulator wafer for mid-infrared photonic integrated circuits," Opt. Express **24**, 11855–11864 (2016).
37. W. Li, P. Anantha, S. Bao, K. H. Lee, X. Guo, T. Hu, L. Zhang, H. Wang, R. Soref, and C. S. Tan, "Germanium-on-silicon nitride waveguides for mid-infrared integrated photonics," Appl. Phys. Lett. **109**, 241101 (2016).
38. S. Khan, J. Chiles, J. Ma, and S. Fathpour, "Silicon-on-nitride waveguides for mid- and near-infrared integrated photonics," Appl. Phys. Lett. **102**, 121104 (2013).
39. T. Baehr-Jones, A. Spott, R. Ilic, A. Spott, B. Penkov, W. Asher, and M. L. Hochberg, "Silicon-on-sapphire integrated waveguides for the mid-infrared," Opt. Express **18**, 12127–12135 (2010).
40. F. Li, S. D. Jackson, C. Grillet, E. Magi, D. Hudson, S. J. Madden, Y. Moghe, C. O'Brien, A. Read, S. G. Duvall, P. Atanackovic, B. J. Eggleton, and D. J. Moss, "Low propagation loss silicon-on-sapphire waveguides for the mid-infrared," Opt. Express **19**, 15212–15220 (2011).
41. M. Brun, P. Labeye, G. Grand, J.-M. Hartmann, F. Boulila, M. Carras, and S. Nicoletti, "Low loss SiGe graded index waveguides for mid-IR applications," Opt. Express **22**, 508–518 (2014).
42. P. T. Lin, H. Jung, L. C. Kimerling, A. Agarwal, and H. X. Tang, "Low-loss aluminium nitride thin film for mid-infrared microphotonics," Laser Photon. Rev. **8**, L23–L28 (2014).
43. Z. Cheng, X. Chen, C. Y. Wong, K. Xu, and H. K. Tsang, "Broadband focusing grating couplers for suspended-membrane waveguides," Opt. Lett. **37**, 5181–5183 (2012).
44. Z. Cheng, X. Chen, C. Y. Wong, K. Xu, C. K. Y. Fung, Y. M. Chen, and H. K. Tsang, "Focusing subwavelength grating coupler for mid-infrared suspended membrane waveguide," Opt. Lett. **37**, 1217–1219 (2012).
45. Z. Cheng, X. Chen, C. Y. Wong, K. Xu, C. K. Y. Fung, Y. M. Chen, and H. K. Tsang, "Mid-infrared grating couplers for silicon-on-sapphire waveguides," IEEE Photon. J. **4**, 104–113 (2012).
46. C. Alonso-Ramos, M. Nedeljkovic, D. Benedikovic, J. S. Penades, C. G. Littlejohns, A. Z. Khokhar, D. Perez-Galacho, L. Vivien, P. Cheben, and G. Z. Mashanovich, "Germanium-on-silicon mid-infrared grating couplers with low-reflectivity inverse taper excitation," Opt. Lett. **41**, 4324–4327 (2016).
47. Y. Wei, G. Li, Y. Hao, Y. Li, J. Yang, M. Wang, and X. Jiang, "Long-wave infrared 1×2 MMI based on air-gap beneath silicon rib waveguides," Opt. Express **19**, 15803–15809 (2011).
48. M. M. Milošević, M. Nedeljkovic, T. M. B. Masaud, E. Jaberansary, H. M. H. Chong, G. T. Reed, and G. Z. Mashanovich, "Submicron silicon waveguides and optical splitters for mid-infrared applications," in *9th International Conference on Group IV Photonics (GFP)* (2012), paper WA5.
49. M. Nedeljkovic, A. Z. Khokhar, Y. Hu, X. Chen, J. Soler Penades, S. Stankovic, H. M. H. Chong, D. J. Thomson, F. Y. Gardes, G. T. Reed, and G. Z. Mashanovich, "Silicon photonic devices and platforms for the mid-infrared," Opt. Mater. Express **3**, 1205–1214 (2013).
50. A. Malik, M. Muneeb, Y. Shimura, J. V. Campenhout, R. Loo, and G. Roelkens, "Germanium-on-silicon mid-infrared waveguides and Mach-Zehnder interferometers," in *IEEE Photonics Conference (IPC)* (2013), paper MF1.4.
51. A. Spott, Y. Liu, T. Baehr-Jones, R. Ilic, and M. Hochberg, "Silicon waveguides and ring resonators at 5.5 μm," Appl. Phys. Lett. **97**, 213501 (2010).
52. C. Y. Wong, Z. Cheng, X. Chen, K. Xu, C. K. Y. Fung, Y. M. Chen, and H. K. Tsang, "Characterization of mid-infrared silicon-on-sapphire microring resonators with thermal tuning," IEEE Photon. J. **4**, 1095–1102 (2012).
53. R. Shankar, I. Bulu, and M. Lončar, "Integrated high-quality factor silicon-on-sapphire ring resonators for the mid-infrared," Appl. Phys. Lett. **102**, 051108 (2013).
54. R. Shankar, R. Leijssen, I. Bulu, and M. Lončar, "Mid-infrared photonic crystal cavities in silicon," Opt. Express **19**, 5579–5586 (2011).
55. C. P. Ho, P. Pitchappa, P. Kropelnicki, J. Wang, Y. Gu, and C. Lee, "Development of polycrystalline silicon based photonic crystal membrane for mid-infrared applications," IEEE J. Sel. Top. Quantum Electron. **20**, 4900107 (2014).
56. Y. Zou, S. Chakravarty, and R. T. Chen, "Mid-infrared silicon-on-sapphire waveguide coupled photonic crystal microcavities," Appl. Phys. Lett. **107**, 081109 (2015).
57. A. Malik, M. Muneeb, S. Pathak, Y. Shimura, J. V. Campenhout, R. Loo, and G. Roelkens, "Germanium-on-silicon mid-infrared arrayed waveguide grating multiplexers," IEEE Photon. Technol. Lett. **25**, 1805–1808 (2013).
58. A. Malik, M. Muneeb, Y. Shimura, J. V. Campenhout, R. Loo, and G. Roelkens, "Germanium-on-silicon planar concave grating wavelength (de)multiplexers in the mid-infrared," Appl. Phys. Lett. **103**, 161119 (2013).
59. P. Barritault, M. Brun, P. Labeye, J.-M. Hartmann, F. Boulila, M. Carras, and S. Nicoletti, "Design, fabrication and characterization of an AWG at 4.5 μm," Opt. Express **23**, 26168–26181 (2015).
60. J. S. Penades, Y. Hu, M. Nedeljkovic, C. G. Littlejohns, A. Z. Khokhar, C. J. Mitchell, S. Stankovic, G. Roelkens, F. Y. Gardes, and G. Z. Mashanovich, "Angled MMI CWDM structure on germanium on silicon," in *European Conference on Lasers and Electro-Optics* (2015), paper CK_7_2.
61. T. Hu, M. S. Rouifed, H. Qiu, X. Guo, C. G. Littlejohns, C. Liu, and H. Wang, "A polarization splitter and rotator based on a partially etched grating-assisted coupler," IEEE Photon. Technol. Lett. **28**, 911–914 (2016).
62. T. Hu, H. Qiu, Z. Zhang, X. Guo, C. Liu, M. S. Rouifed, C. G. Littlejohns, G. T. Reed, and H. Wang, "A compact ultrabroadband polarization beam splitter utilizing a hybrid plasmonic Y-branch," IEEE Photon. J. **8**, 4802209 (2016).
63. M. A. V. Camp, S. Assefa, D. M. Gill, T. Barwicz, S. M. Shank, P. M. Rice, T. Topuria, and W. M. J. Green, "Demonstration of electrooptic modulation at 2165 nm using a silicon Mach-Zehnder interferometer," Opt. Express **20**, 28009–28016 (2012).
64. D. J. Thomson, L. Shen, J. J. Ackert, E. Huante-Ceron, A. P. Knights, M. Nedeljkovic, A. C. Peacock, and G. Z. Mashanovich, "Optical detection and modulation at 2 μm-2.5 μm in silicon," Opt. Express **22**, 10825–10830 (2014).
65. L. Shen, N. Healy, C. J. Mitchell, J. S. Penades, M. Nedeljkovic, G. Z. Mashanovich, and A. C. Peacock, "Mid-infrared all-optical modulation in low-loss germanium-on-silicon waveguides," Opt. Lett. **40**, 268–271 (2015).
66. J. Ding, H. Chen, L. Yang, L. Zhang, R. Ji, Y. Tian, W. Zhu, Y. Lu, P. Zhou, R. Min, and M. Yu, "Ultra-low-power carrier-depletion Mach-Zehnder silicon optical modulator," Opt. Express **20**, 7081–7087 (2012).
67. J. Ding, R. Ji, L. Zhang, and L. Yang, "Electro-optical response analysis of a 40 Gb/s silicon Mach-Zehnder optical modulator," J. Lightwave Technol. **31**, 2434–2440 (2013).
68. J. Chiles and S. Fathpour, "Mid-infrared integrated waveguide modulators based on silicon-on-lithium-niobate photonics," Optica **1**, 350–355 (2014).
69. S. Liu, K. Xu, Q. Song, Z. Cheng, and H. K. Tsang, "Design of mid-infrared electro-optic modulators based on aluminum nitride waveguides," J. Lightwave Technol. **34**, 3837–3842 (2016).
70. S. J. Park, A. Zakar, V. L. Zerova, D. Chekulaev, L. T. Canham, and A. Kaplan, "All-optical modulation in mid-wavelength infrared using porous Si membranes," Sci. Rep. **6**, 30211 (2016).
71. M. Nedeljkovic, S. Stankovíc, C. J. Mitchell, A. Z. Khokhar, S. A. Reynolds, D. J. Thomson, F. Y. Gardes, C. G. Littlejohns, G. T. Reed, and G. Z. Mashanovich, "Mid-infrared thermo-optic modulators in SOI," IEEE Photon. Technol. Lett. **26**, 1352–1355 (2014).
72. C. Lin, M. Grau, O. Dier, and M.-C. Amann, "Low threshold room-temperature continuous-wave operation of 2.24–3.04 μm

GaInAsSb/AlGaAsSb quantum-well lasers," Appl. Phys. Lett. **84**, 5088–5090 (2004).
73. L. Shterengasa, G. Belenky, T. Hosoda, G. Kipshidze, and S. Suchalkin, "Continuous wave operation of diode lasers at 3.36 μm at 12°C," Appl. Phys. Lett. **93**, 011103 (2008).
74. S. Belahsene, L. Naehle, M. Fischer, J. Koeth, G. Boissier, P. Grech, G. Narcy, A. Vicet, and Y. Rouillard, "Laser diodes for gas sensing emitting at 3.06 μm at room temperature," IEEE Photon. Technol. Lett. **22**, 1084–1086 (2010).
75. Y. Yao, A. J. Hoffman, and C. F. Gmachl, "Mid-infrared quantum cascade lasers," Nat. Photonics **6**, 432–439 (2012).
76. M. Razeghi, Q. Y. Lu, N. Bandyopadhyay, W. Zhou, D. Heydari, Y. Bai, and S. Slivken, "Quantum cascade lasers: from tool to product," Opt. Express **23**, 8462–8475 (2015).
77. M. S. Vitiello, G. Scalari, B. Williams, and P. D. Natale, "Quantum cascade lasers: 20 years of challenges," Opt. Express **23**, 5167–5182 (2015).
78. G. Maisons, C. Gilles, L. Orbe, G. Carpintero, J. Abautret, and M. Carras, "Monolithic integration of a widely-tunable mid-infrared source based on DFB QCL array and echelle grating," in *Laser Applications to Chemical, Security and Environmental Analysis* (2016), paper LTh3E.7.
79. A. Spott, J. Peters, M. L. Davenport, E. J. Stanton, C. D. Merritt, W. W. Bewley, I. Vurgaftman, C. S. Kim, J. R. Meyer, J. Kirch, L. J. Mawst, D. Botez, and J. E. Bowers, "Quantum cascade laser on silicon," Optica **3**, 545–551 (2016).
80. S. Latkowski, A. Hänsel, P. J. van Veldhoven, D. D'Agostino, H. Rabbani-Haghighi, B. Docter, N. Bhattacharya, P. J. A. Thijs, H. P. M. M. Ambrosius, M. K. Smit, and K. A. Williams, "Monolithically integrated widely tunable laser source operating at 2 μm," Optica **3**, 1412–1417 (2016).
81. A. Gassenq, F. Gencarelli, J. Van Campenhout, Y. Shimura, R. Loo, G. Narcy, B. Vincent, and G. Roelkens, "GeSn/Ge heterostructure short-wave infrared photodetectors on silicon," Opt. Express **20**, 27297–27303 (2012).
82. H. Cong, C. Xue, J. Zheng, F. Yang, K. Yu, Z. Liu, X. Zhang, B. Cheng, and Q. Wang, "Silicon based GeSn p-i-n photodetector for SWIR detection," IEEE Photon. J. **8**, 1–6 (2016).
83. J. Wang, J. Hu, P. Becla, A. M. Agarwal, and L. C. Kimerling, "Resonant-cavity-enhanced mid-infrared photodetector on a silicon platform," Opt. Express **18**, 12890–12896 (2010).
84. J. Wang, T. Zens, J. Hu, P. Becla, L. C. Kimerling, and A. M. Agarwal, "Monolithically integrated, resonant-cavity-enhanced dual-band mid-infrared photodetector on silicon," Appl. Phys. Lett. **100**, 211106 (2012).
85. J. Wu, Q. Jiang, S. Chen, M. Tang, Y. I. Mazur, Y. Maidaniuk, M. Benamara, M. P. Semtsiv, W. T. Masselink, K. A. Sablon, G. J. Salamo, and H. Liu, "Monolithically integrated InAs/GaAs quantum dot mid-infrared photodetectors on Si substrates," ACS Photon. **3**, 749–753 (2016).
86. X. Luo, Y. Cheng, J. Song, T.-Y. Liow, Q. J. Wang, and M. Yu, "Wafer-scale dies-transfer bonding technology for hybrid III/V-on-silicon photonic integrated circuit application," IEEE J. Sel. Top. Quantum Electron. **22**, 443–454 (2016).
87. H. Jane and R. P. Tatam, "Optical gas sensing: a review," Meas. Sci. Technol. **24**, 012004 (2012).
88. Z. Han, P. Lin, V. Singh, L. Kimerling, J. Hu, K. Richardson, A. Agarwal, and D. T. H. Tan, "On-chip mid-infrared gas detection using chalcogenide glass waveguide," Appl. Phys. Lett. **108**, 141106 (2016).
89. C. J. Smith, R. Shankar, M. Laderer, M. B. Frish, M. Loncar, and M. G. Allen, "Sensing nitrous oxide with QCL-coupled silicon-on-sapphire ring resonators," Opt. Express **23**, 5491–5499 (2015).
90. B. E. Little, S. T. Chu, H. A. Haus, J. Foresi, and J. P. Laine, "Microring resonator channel dropping filters," J. Lightwave Technol. **15**, 998–1005 (1997).
91. J. Song, X. Luo, X. Tu, M. K. Park, J. S. Kee, H. Zhang, M. Yu, G.-Q. Lo, and D.-L. Kwong, "Electrical tracing-assisted dual-microring label-free optical bio/chemical sensors," Opt. Express **20**, 4189–4197 (2012).
92. A. Glière, J. Rouxel, M. Brun, B. Parvitte, V. Zéninari, and S. Nicoletti, "Challenges in the design and fabrication of a lab-on-a-chip photoacoustic gas sensor," Sensors **14**, 957–974 (2014).